PHYSICAL REVIEW B **72**, 174104 (2005)

Local structure in $LaMnO_3$ and $CaMnO_3$ perovskites: A quantitative structural refinement of Mn *K*-edge XANES data

C. Monesi,[1] C. Meneghini,[1,2,*] F. Bardelli,[1,2] M. Benfatto,[3] S. Mobilio,[1,2,3] U. Manju,[4] and D. D. Sarma[4]
[1]*Dipartimento di Fisica Universitá di "Roma Tre," Via della Vasca Navale 84, I-00146 Roma, Italy*
[2]*INFM-GILDA c/o ESRF Grenoble, France*
[3]*INFN Laboratori Nazionali di Frascati, Via E. Fermi 40, I-00044 Frascati, Italy*
[4]*Solid State and Structural Chemistry Unit, Indian Institute of Science, Bangalore 560012, India*
(Received 18 May 2005; published 7 November 2005)

Hole-doped perovskites such as $La_{1-x}Ca_xMnO_3$ present special magnetic and magnetotransport properties, and it is commonly accepted that the local atomic structure around Mn ions plays a crucial role in determining these peculiar features. Therefore experimental techniques directly probing the local atomic structure, like x-ray absorption spectroscopy (XAS), have been widely exploited to deeply understand the physics of these compounds. Quantitative XAS analysis usually concerns the extended region [extended x-ray absorption fine structure (EXAFS)] of the absorption spectra. The near-edge region [x-ray absorption near-edge spectroscopy (XANES)] of XAS spectra can provide detailed complementary information on the electronic structure and local atomic topology around the absorber. However, the complexity of the XANES analysis usually prevents a quantitative understanding of the data. This work exploits the recently developed MXAN code to achieve a quantitative structural refinement of the Mn *K*-edge XANES of $LaMnO_3$ and $CaMnO_3$ compounds; they are the end compounds of the doped manganite series $La_xCa_{1-x}MnO_3$. The results derived from the EXAFS and XANES analyses are in good agreement, demonstrating that a quantitative picture of the local structure can be obtained from XANES in these crystalline compounds. Moreover, the quantitative XANES analysis provides topological information not directly achievable from EXAFS data analysis. This work demonstrates that combining the analysis of extended and near-edge regions of Mn *K*-edge XAS spectra could provide a complete and accurate description of Mn local atomic environment in these compounds.

DOI: 10.1103/PhysRevB.72.174104 PACS number(s): 61.10.Ht, 75.47.Lx, 73.43.Qt

I. INTRODUCTION

Due to their peculiar magnetic, electronic, and transport properties a large number of theoretical and experimental studies were dedicated in the last two decades to manganese oxides with perovskite structure. Such materials are in fact of interest both for technological applications and for fundamental research in the field of strongly correlated systems. Their peculiar properties arise from a strong interplay between ferromagnetic double-exchange (DE) interaction[1–3] among Mn ions, antiferromagnetic superexchange (SE) among the same ions, and strong electron-phonon interaction (small and/or large polarons),[4,5] which results in a complex phase diagram in terms of structural, magnetic, and electronic properties as a function of composition, temperature, and pressure.[6]

It was clearly demonstrated that the local atomic structure around Mn ions plays a crucial role[7–9] in determining these complex phenomena, mainly because the electron-phonon coupling involves a dynamical Jahn-Teller deformation of the Mn local surroundings. For this reason short-range-order techniques like x-ray absorption spectroscopy[10] (XAS) are very well suited for studying these compounds and, as a matter of fact, a number of XAS studies on manganese perovskite oxides[11–16] have been reported in the literature; many of them obtained valuable information from a quantitative analysis of the extended region of the spectra, the so-called extended x-ray absorption fine structure (EXAFS) region. On the contrary fewer experimental works exist that quantitatively analyze the near-edge region of the XAS spectra, known as the x-ray absorption near-edge fine structure (XANES) region, from a structural point of view.[17–22] Nevertheless, the analysis of XANES can provide, in principle, very fine details of the local structure around the absorber, so contributing to the full understanding of the peculiar physical properties of these materials. In fact the low-energy part of an absorption spectrum, which extends from the edge to about 50–100 eV above it (edge and near-edge regions), resembles the local electronic density of states close to the Fermi level giving information on the charge state of the absorbing atom; moreover, it provides information on the symmetry and topological features of the local atomic environment[23] which are complementary to the EXAFS ones. XANES features are usually interpreted in terms of the scattering processes of the ejected photoelectron as for the EXAFS data, but now multiple scattering of the photoelectron gives a large contribution.[23,24] This makes the XANES highly sensitive to the topology of the atomic environment around the absorber so that, in principle, the XANES analysis allows recovering the detailed three-dimensional (3D) local structure around the absorber. In mixed-oxide manganites a detailed, quantitative analysis of XANES would provide valuable information: it is well known that in these compounds the local structure around Mn ions may sensibly differ from that derived from crystallographic probes. Nevertheless, the large amount of information present in the spectra makes the quantitative interpretation of XANES data a very complex task. This is the reason why the experimental works on XANES generally report qualitative or semiquantitative structural information.

Some codes exist to calculate XANES spectra for given atomic clusters, the most widely used being the FEFF software package.[25] In such codes a local structure around the absorber is assumed, and on its basis the potential acting on the photoelectron is calculated in the muffin-tin approximation and then used to solve the Schrödinger equation in the multiple-scattering formalism; finally, the absorption cross section is evaluated. Such a procedure produced very good results in many different systems, but does not allow one to reconstruct the local structure around the absorber in a quantitative way—i.e., through a best fitting procedure on the structural parameters.

Recently an innovative code, named MXAN,[26,27] was developed which allows such a quantitative reconstruction. MXAN calculates the theoretical x-ray photoabsorption cross section as previously outlined and then fits it to the experimental data by refining the structural parameters. It was successfully applied to ionic solutions and biological samples,[28,29] getting new insight into the local structure in these compounds. This work is aimed at proving the possibility to extend this kind of analysis to crystalline (long-range-ordered) systems and, in particular, to the manganites, in which the local and crystallographic structures may differ. In this work we report the quantitative structural refinement of the local structure around Mn in $LaMnO_3$ and $CaMnO_3$, the two end compounds of the doped manganite series $La_xCa_{1-x}MnO_3$, in which the Mn atoms are present only in one charge state as Mn^{3+} and Mn^{4+}, respectively. The structural refinement was achieved by analyzing XANES data at the Mn K edge with MXAN code; the structural parameters obtained resulted to be in very good agreement with those derived from the EXAFS part of the spectra, showing how a quantitative picture of the local structure can be obtained from XANES in such crystalline materials. In addition XANES provided additional topological information on the bond angle distributions. The very good results attained on these two end compounds open a way to extend this approach to the mixed oxides, where the mixed-valence states of Mn^{3+} and Mn^{4+} provide special physical properties.

II. EXPERIMENTAL AND DATA ANALYSIS

Soft chemistry procedures have been employed to prepare the stoichiometric $LaMnO_3$ and $CaMnO_3$ oxides. Stoichiometric amounts of analytical-grade La_2O_3, $Ca(NO_3)_2$, and $MnCO_3$ were dissolved in citric acid. The citrate solutions were slowly evaporated, leading to organic resins containing a random distribution of the involved cations at an atomic level. All the organic materials were eliminated in a treatment at 700 °C in air, for 12 h. This treatment gave highly reactive precursor materials, amorphous to x-ray diffraction (XRD). $LaMnO_3$ precursor was then treated at 1100 °C in a N_2 flow for 12 h to avoid the oxidation of the samples. $CaMnO_3$ precursor was annealed in air at 1100 °C for 12 h. All the compounds appear well crystallized, single phase at standard x-ray diffraction analysis. Samples for XAS experiments were kept in vacuum to prevent degradation.

Sample pellets were gently ground by hand in agata mortar under ethylic alcohol. The powders where suspended in ethylic alcohol under an ultrasonic bath, and then the finest powders were deposited onto a Millipore membrane and enclosed between two Kapton tape films.

Mn K-edge x-ray absorption spectra were recorded at the GILDA-BM8 beamline of the European Synchrotron Radiation Facility (ESRF).[30] The x-ray beam was monochromatized by a Si[311] double-crystal fixed exit and sagittal focussing monochromator; a couple of grazing incidence mirrors placed before the sample were used to clean the x-ray beam from higher-order harmonics (energy cut off at about 10 keV). The absorption spectra were collected in the energy range 6150–7700 eV in transmission mode at liquid nitrogen temperature to reduce the effect of thermal disorder. Incident (I_0) and transmitted (I_1) x-ray intensities were measured by N_2-filled ionization chambers. Standard procedures were adopted for data normalization and extraction of the EXAFS structural signal. The pre-edge behavior was simulated with a straight line, fitting the data in the range 6150–6500 eV. The origin of the photoelectron energy scale (E_0) was chosen at the maximum of the first derivative of $\mu(E)$ and refined during the fitting (see below). The post-edge atomic absorption background (μ_0) was calculated by fitting a polynomial spline to the data in the energy range 6570–7700 eV, corresponding to the k range $k \approx 2.3$–18 Å^{-1} [being $k = \hbar^{-1}\sqrt{2m(E-E_0)}$]. The structural EXAFS signal was finally calculated as

$$\chi^{expt}(k) = \frac{\mu(k) - \mu_0(k)}{\mu_0(k)}.$$

III. DATA ANALYSIS AND RESULTS

A. Exafs

EXAFS data analysis was performed by fitting the experimental data with the standard formula[10]

$$k\chi(k) = S_0^2 \sum_i N_i \frac{A_{0i}\sin(2kR_i + \phi_{0i})}{R_i^2} e^{2R_i/\lambda_i} e^{-2k^2\sigma_i^2}, \qquad (1)$$

in which the sum runs over single- (SS) and multiple- (MS) scattering contributions. For the ith signal (SS or MS) the standard formula (1) assumes a Gaussian distribution of the atoms, giving rise to a photoelectron effective scattering path with average length R_i and variance σ_i, N_i being the multiplicity of the contribution. The $A_{0i}(k)$ and $\phi_{0i}(k)$ are, respectively, the total amplitude and phase factors for the ith contribution. The $\lambda_i(k)$ is the photoelectron mean free path, and S_0^2 is a global factor taking into account many-body losses. The amplitude and phase functions were calculated by FEFF8.2 (Ref. 31) in the muffin-tin approximation using complex Hedin-Lundqvist empirical potentials and assuming the crystallographic structure of $CaMnO_3$ (Ref. 32) and $LaMnO_3$ (Ref. 33) (antiferromagnetic P_{nma} phase at about 100 K) as structural models.

The EXAFS data were analyzed in the k range 3–17 Å^{-1} according to the prescription of the *XAS standards and cri-*

teria committee.[34] The fitting minimizes the k^n-weighted square residual function:

$$\mathrm{Res}^2_\chi = \frac{1}{N}\sum_j \left(\frac{k^n(\chi_j^{th}(k) - \chi_j^{expt}(k))}{w_j(k)}\right)^2,$$

where the sum runs over the N experimental points; k weight $n=2$ was used for both $CaMnO_3$ and $LaMnO_3$ samples. The uncertainty in each measured data point, $w_j(k)$, was calculated as $w_j(k)=|\chi_j^{exp}(k)-\bar{\chi}_j(k)|$ where $\bar{\chi}_j$ is a smooth high-degree polynomial spline through the experimental data. The average uncertainty in experimental data $\bar{w}$ resulted in being better than 7×10^{-4}.

After some preliminary checks in fitting the EXAFS data the S_0^2 was fixed to 0.85; the theoretical mean free path $\lambda(k)$ calculated by the FEFF8.2 code was used without further corrections. All the two-body signals (single-scattering contributions) derived from the crystallographic models up to about 7 Å were considered. The multiplicity numbers of each signal were fixed to their crystallographic values; therefore, each SS contribution requires only two free parameters: namely, R_i and σ_i^2. Multiple-scattering contributions are generally weak in the extended region but they can largely increase when the scatters are aligned due to the so-called focousing effect, which enhances the forward-scattering amplitude.[10] The MS contributions were considered up to triple-scattering terms (i.e., four-leg paths) only for the almost collinear configurations (i.e., bond angles >140°) and were introduced according to their relative intensity, as calculated by the FEFF code. As before the multiplicity of MS terms was fixed to the crystallographic value.

An accurate error analysis was performed in order to determine the confidence limits on the refined parameters and the covariance matrix using the MINUT capabilities.[35] In order to reduce the correlation among the parameters and to define the minimal set of contributions and parameters able to fit the data we proceeded as follows: first (a) the energy scale (E_0) and the Debye-Waller factors (σ_i^2) were refined keeping fixed the R_i values, then (b) the R_i were adjusted keeping fixed E_0 and σ_i^2; the refinement cycles through a and b. At each cycle the contributions whose R_i differs less than about 5% are gathered together in a single one; the significance of weak contributions (i.e., with a large σ_i^2) is statistically checked with the F test and eventually removed. Finally all the parameters for the remaining contributions are refined at the same time.

TABLE I. Mn-local structure on $CaMnO_3$ and $LaMnO_3$ samples as resulting from EXAFS analysis. The errors in the last digit of the refined parameters are reported in parentheses.

	$CaMnO_3$			
	SS	N	R (Å)	σ^2 ($\times10^{-3}$Å^2)
(1)	Mn-O_1	6	1.895 (3)	3.3 (4)
(2)	Mn-Ca_1	8	3.18 (1)	15. (2)
(3)	Mn-Mn_2	12	5.29 (2)	9.6 (36)
(4)	Mn-O_3	24	5.53 (2)	9.2 (19)
(5)	Mn-Ca_2	24	6.07 (3)	16.0 (5)
	MS	N	δ (Å)	σ^2 ($\times10^{-3}$Å^2)
(6)	Mn-O_1-Mn_1	6	0.039 (6)	5.8 (12)
(7)	Mn-Mn_3	8	-	(S_3) 12.0 (3)
			ΔE=0.9 (5) eV χ^2_ν=0.83 (ν=14)	
	$LaMnO_3$			
	SS	N	R (Å)	σ^2 ($\times10^{-3}$Å^2)
(1)	Mn-O_p	4	1.921 (4)	1.8 (5)
(2)	Mn-O_a	2	2.129 (9)	1.8
(3)	Mn-La_{1a}	6	3.35 (2)	12.0 (2)
(4)	Mn-La_{1b}	2	3.66 (1)	4.2 (9)
(5)	Mn-Mn_2	12	5.54 (2)	5.3 (13)
(6)	Mn-La_3	24	6.67 (4)	7.9 (26)
	MS	N	δ (Å)	σ^2 ($\times10^{-3}$Å^2)
(9)	Mn-O_1-Mn_1	6	0.0027 (9)	(S_2) 13.0 (3) (S_3) 9.7 (32)
(7)	Mn-Mn_3	8	-	(S_3) 6.9 (29)
			ΔE=−0.7(6) eV χ^2_ν=0.86(ν=16)	

The $CaMnO_3$ EXAFS data were fitted with 7 contributions (Table I): 5 are single scattering from (see Fig. 1) six oxygen ion nearest neighbors (O_1), 8 Ca ions at the center of the pseudocubic unit (Ca_1), 12 Mn ions on the diagonal of pseudo cube faces (Mn_2), 24 oxygen ions on the opposite pseudo cube edges (O_3), and 24 Ca ions on the center of next pseudo cube units. Only two MS contributions were found to give relevant signal: namely, the Mn—O_1-Mn_1 configuration along the cube edges and Mn—Ca_1-Mn_3 along the cube diagonal. The contributions from O_2 ion (Fig. 1) are found to be negligible. Both the above MS contributions to the signal A-B-C (A being the Mn absorber) are made of three terms: the single scattering (from $A\leftrightarrows C$ photoelectron paths), double scattering S_2 (from $A \underset{\leftarrow B\leftarrow}{\longrightarrow} C$ and $A \underset{\rightarrow B\rightarrow}{\longleftarrow} C$ photoelectron paths), and triple scattering S_3 (from $A\leftrightarrows B\leftrightarrows C$ photoelectron paths). The structural parameters of these three terms are correlated since all refers to the same A-B-C triangle and the A-B and B-C distances must be that found for Mn-O_1 nearest-neighbor configurations. For these reasons we constrained the photo electron path length for S_3 to the Mn-O nearest-neighbor distance: $R_{S_3}=2R_{MnO_1}$. We have introduced the quantity δ defined as $\delta=R_{S_3}-R_{S_2}$; in terms of δ the long leg R_{AC} is $R_{AC}=R_{S_3}-2\delta$. Therefore the $\widehat{A\text{-}B\text{-}C}$ bond angle is given by $\theta_B=2\sin^{-1}[(R_{S_3}-2\delta)/R_{S_3}]$. As for the Mn-$O_1$-$Mn_1$ configurations, the Debye-Waller factors of single-, double-, and triple-scattering contributions are heavy correlated and, if refined together, produce errors as large as 80%; therefore we used the same Debye-Waller factor for the three contributions. Concerning the contribution

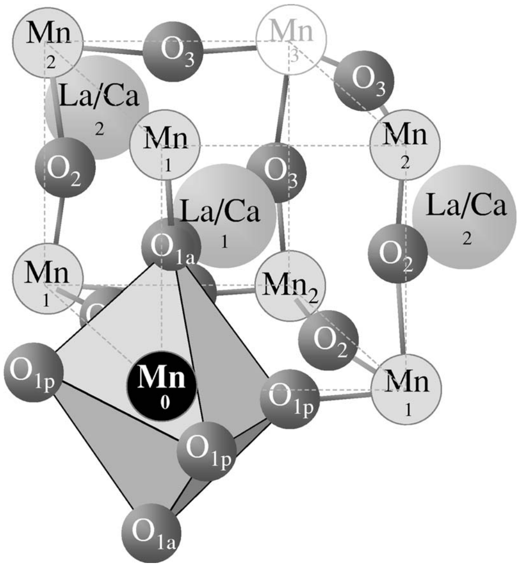

FIG. 1. Schematic view of La(Ca)MnO_3 structure. The generic Mn absorber ion (Mn_0) is presented in black.

Mn-Ca_1-Mn_2, it is dominated by the S_3 while the SS and S_2 terms were found negligible and were not considered in the final refinement. This procedure gives a satisfactory best fit in the k range 3–17 Å^{-1}, well reproducing the main structural features of the Fourier transform up to about 7 Å (Fig. 2). Including the energy scale (E_0) 14 free parameters were refined in the fitting (Table I), giving a final reduced $\chi^2_\nu \sim 0.8$.

The analysis of $LaMnO_3$ data is more complex due to the large Jahn-Teller distortion around the Mn^{3+}, which results in a larger structural disorder. To fit the EXAFS data six SS and two MS contributions were required (Table I). The nearest-neighbor shell is fitted with two contributions to take into account the Jahn-Teller (JT) deformation of the MnO_6 octahedra. The same Debye-Waller factor was used for planar (Mn-O_p) and apical (Mn-O_a) neighbors. This is an arbitrary choice but it is mandatory in order to avoid the huge correlation between the disorder factor of these two subshells. Also the Mn-La_1 distribution was fitted using two independent shells: Mn-La_{1a} and Mn-La_{1b} with multiplicity 6 and 2, respectively. The Mn-O_2 and Mn-O_3 give negligible contributions, probably due to their very broad distributions and weakness of the Mn-O backscattering amplitude with respect to the other terms. The contributions of Mn-O_1-Mn_1 and Mn-La_1-Mn_3 (SS and MS) were treated as for $CaMnO_3$ using the average Mn-O_1 and Mn-La_1 distances in the calculation of MS terms. Concerning the Mn-O_1-Mn_1 we found the SS contribution (Mn-Mn_1) negligibly small (huge Debye-Waller term) and it was neglected in the final fit. The σ^2 for S_2 and S_3 were refined independently. As before the Mn-La_1-Mn_3 configuration only contributes with S_3 term while the SS and S_2 were neglected in the final refinement.

Also in this case, the procedure gives a satisfactory best fit in the k range 3–17 Å^{-1} and well reproduces the main structural features of the Fourier transform up to about 7 Å (Fig. 2). Including the energy scale (E_0) 16 free parameters were refined in the fitting (Table I), giving a final $\chi^2_\nu \sim 0.9$.

In general the best fit in $LaMnO_3$ sample is slightly worse than in $LaMnO_3$, reflecting the more complex Mn local structure in this sample.

B. Xanes

The XANES analysis concerned the energy region from 10 eV below the edge up to 180 eV above the edge. The experimental spectra, after subtraction of the pre-edge, were normalized to the jump edge. The MXAN code was used to fit the calculated x-ray absorption cross section $\mu_{th}(E)$ to the experimental data. The MXAN procedures are well detailed in Refs. 26 and 27; here, we recall the main features for sake of completeness.

MXAN calculates the x-ray absorption cross section using the CONTINUUM package developed by the theory group of the LNF (Laboratori Nazionali di Frascati) of the INFN (Istituto Nazionale di Fisica Nucleare).[36] The calculation is made in the full multiple-scattering scheme using the muffin-tin approximation for the shape of the atomic potentials. The real part of the self-energy was calculated using the Hedin-Lundqvist energy-dependent potentials;[37] since even small changes in the local structure can produce detectable differences in the potential,[26] the potential is recalculated at each step of the fitting procedure. After the calculation a broadening is included convolving the calculated $\mu_{th}(E)$ with an energy-dependent Lorentzian function of width $\Gamma(E)=\Gamma_r+\Gamma_p(E)$. The constant term Γ_r takes into account the core-hole lifetime and the experimental resolution. The energy-dependent term $\Gamma_p(E)$ takes into account the inelastic processes. It is assumed to be zero below the plasmon excitation energy E_{pi} and above it varies from an initial value A_{pi} according the universal function of the mean free path in solids.[38] The convolution of the spectrum with an arc-tangent function eliminates the discontinuity at E_{pi}. The numerical values for $\Gamma_r(E), E_{pi}$, and A_{pi} are optimized at each refinement step of the structural parameters using a simulated annealing procedure based on a Monte Carlo search. Slope correction and normalization are also refinable parameters. The validity of this approach has been demonstrated in detail in Refs. 27 and 29.

The first step in the refinement procedure was the choice of the cluster dimension (number of atoms) around the absorber. This has been performed by progressively adding neighbor shells around the absorber while assuming the crystallographic structure for $LaMnO_3$ and $CaMnO_3$. The optimal balance between computation time and cluster size resulted in an 87-atom cluster: i.e., the absorber, 6 O_1, 6 Mn_1, 24 O_2, 12 Mn_2, 24 O_3, 6 O_4, and 8 Mn_3 (Fig. 1).

The next step was the optimization of the potential and of the normalization parameters: namely, the overlap between the muffin-tin spheres according to the Norman criterium, the Fermi energy, the slope, and the broadening parameters [Fig. 3(a)]. Finally the atomic structure was refined.

After some preliminary tests we chose the groups of atoms to be refined together at each step[44]: (i) the 6 O_1 atoms bound to Mn, (ii) the 8 La_1(Ca_1) ions at the cube center, and (iii) the 6 Mn_1 ions on the cube edges. We found that the

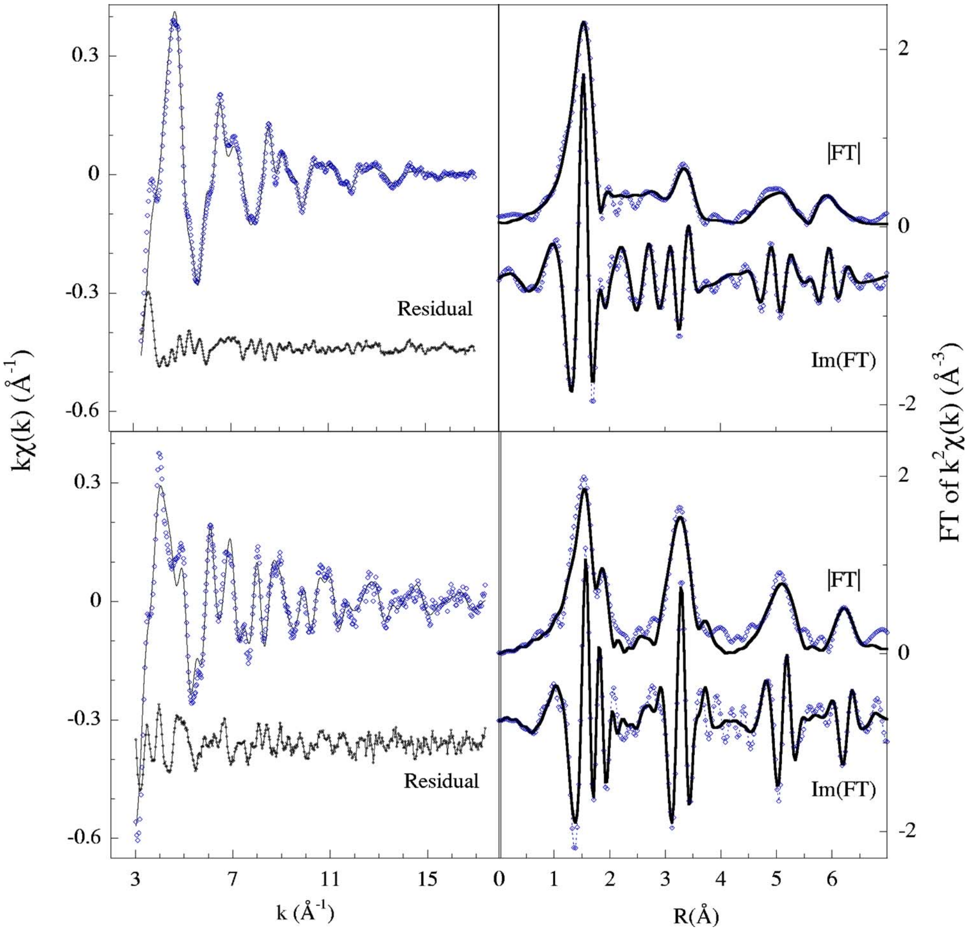

FIG. 2. (Color online) EXAFS fitting results. Left: experimental data (points) and best fit are shown in k space for $CaMnO_3$ (upper panel) and $LaMnO_3$ (lower panel). The residual $k(\chi_{expt}-\chi_{th})$ are shown, shifted for clarity. Right: the moduli and imaginary parts (shifted for clarity) of Fourier transforms of experimental (points) and theoretical (lines) EXAFS data for $CaMnO_3$ (upper panel) and $LaMnO_3$ (lower panel).

refinement of the position of the faraway ions produces large instability of the fitting procedure while having only a weak effect on the best fit accuracy; thus, the positions of these atoms were kept fixed at the crystallographic positions. The fitting proceeded cyclically through the refinement of (i), (ii), and (iii). When a stable configuration is achieved, the potential parameters are recalculated and a new refinement cycle restarted. In our case the 87-atom cluster requires about 24–48 h on a Linux-based workstation equipped with 3 Ghz PIV processor. A complete refinement is achieved in 20–25 cycles,—that is, about 800 h. At the state of the art the long computing time prevents one from fully exploiting the capabilities of MINUIT subroutines for an accurate analysis of statistical errors taking into account the correlations among the parameters. The error bars on the refined parameter were estimated as the variance on a set of different structures producing similar fitting ($\chi^2_\nu < \chi^2_\nu(\text{min}) + 5\%$). In the near future the parallelization of the MXAN code will allow an improvement of the treatment of the errors.

After some refinement cycle a mismatch in the slope between experimental and calculated spectra was evident, preventing a satisfactory refinement: the large residuals found either in $LaMnO_3$ and $CaMnO_3$ XANES [Fig. 3(b)] suggested the presence of a secondary absorption edge in the spectra due to multiple-excitation effects. The relevance of multiple excitation in the analysis of the XAS data has been widely discussed in the literature;[39–41] in the extended region of a XAS spectrum, additional edges can be (partially) masked by a proper choice of the splines that mimic the atomic background, but on the contrary, in the XANES region, the effect of a secondary edge can be dramatic and must be considered. In order to take into account multiple excitations the MXAN code was modified, parametrizing the secondary edge with an arc-tangent function so introducing three additional nonstructural parameters to the fitting: namely, the onset energy (E_{de}), amplitude (A_{de}), and width (W_{de}) of the secondary edge. Adding the contribution of a multiple excitation in this form drastically reduces the residual (Fig. 3). The refined values for E_{de} in the two samples are, respectively, $E_{de}(CaMnO_3)=75\pm4$ eV and $E_{de}(LaMnO_3)=69\pm4$ eV. These values must be compared with the energy positions of the M_I and M_{II} edges of Fe, which in the simple $Z+1$ approximation amounts to about 53 eV.[42] Considering that an additional shift towards higher energy values should be considered for the valence status of Mn in our samples (Mn^{3+} in $LaMnO_3$ and Mn^{4+} in $CaMnO_3$) we can consider satisfactory the agreement we found. Moreover, the positive shift between the $E_{de}(CaMnO_3)$ and $E_{de}(LaMnO_3)$ is consistent with the higher-valence status of Mn in the $CaMnO_3$. Finally we notice that the inclusion of a secondary edge in the fitting reduces the parameter Γ_r (taking into account the core-hole lifetime effect; see above) in both samples: in $LaMnO_3$ the Γ_r decreases from about 2 eV (without secondary edge) to 1.2 eV (with secondary edge) and in $CaMnO_3$ it decreases from about 2.3 eV to about 1.4 eV. These values match well with the Mn core-hole width of

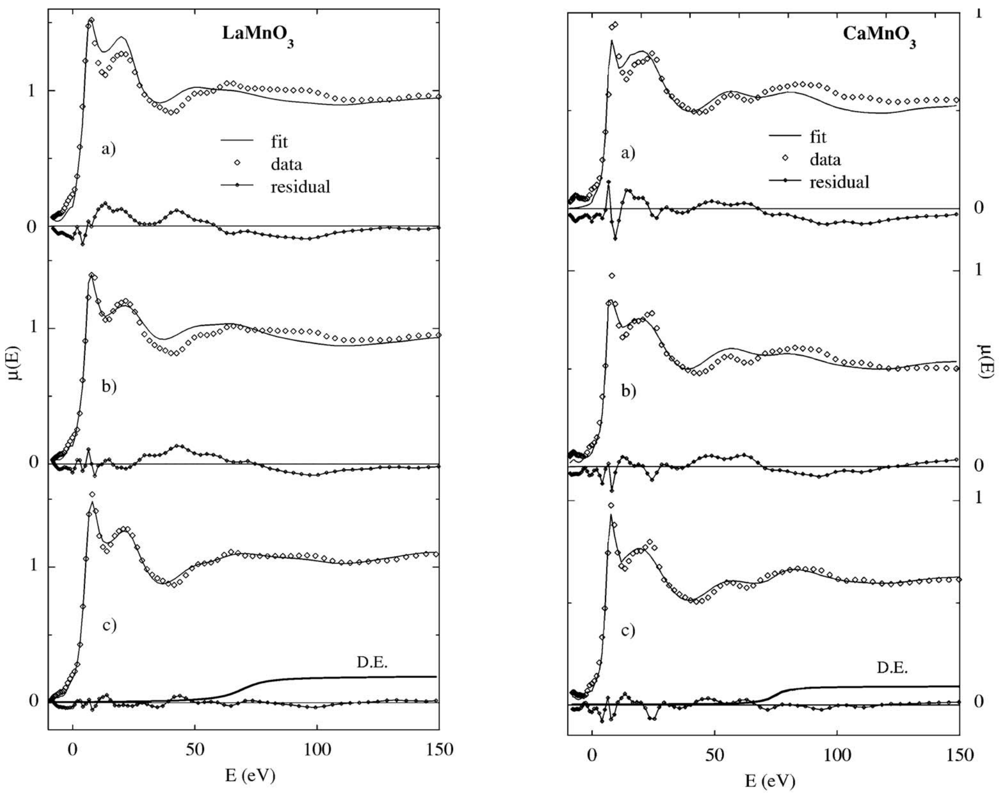

FIG. 3. XANES fitting for $LaMnO_3$ (left panels) and $CaMnO_3$ (right panels): the experimental data (diamonds), the theoretical curves (solid lines), and the residual (experimental and theory, lines and points) are reported, shifted for clarity. Some relevant steps of the refinement procedure are shown, shifted for clarity: (a) The initial model obtained from the crystallographic structure; only the potential parameters are refined (see text). (b) The best fit without secondary edge. In the lower panels (c) the best fit and experimental data are shown; the secondary-edge contributions are also shown, shifted for clarity.

1.16 eV, definitively convincing us of the relevance of the multiple-edge effect in these spectra.

Best fits of XANES for $LaMnO_3$ and $CaMnO_3$ samples are shown in Fig. 3 while the main structural parameters are reported in Table II

IV. RESULTS AND DISCUSSION

The structural data obtained from the extended and near-edge regions of the XAS spectra are compatible between them and in agreement with the crystallographic data of Refs. 32 and 33 (Table III).

The Mn-O_1 distance found by XAS (EXAFS and XANES) in $CaMnO_3$ is in good agreement with the average crystallographic distance. The Mn-O_1 average distance derived from the XANES fitting is slightly longer than the EXAFS one. The XANES results suggest, in addition, a bimodal Mn-O_1 distribution with three shorter (~ 1.904 Å) and three longer (~ 1.924 Å) bonds, in agreement with the crystallographic structure, which shows four shorter bonds at ~ 1.89 Å and two longer bonds at ~ 1.92 Å. The JT distortions $\left[\sigma_{JT}=\sqrt{1/6\Sigma_{i=1}^{6}(R_i-\bar{R})}\right]$ given from crystallography and from XANES are the same. The XANES analysis also confirms that the six O_1 neighbors are effectively in an octahedral configuration around Mn with O_1-Mn_0-O_1 bond angles θ_{Mn} equal to 90°. with a sharp distribution $\sigma_{\theta}^{2}\sim 3°$. These topological information cannot be directly obtained from the EXAFS data analysis due to its weak multiple-scattering signal in the extended region. Even the average Mn-O_1-Mn_1 bond angles (θ_{O_1}) found by XANES and diffraction are the same and the bond angle distribution width (σ_θ) from XANES analysis is in good agreement with the crystallographic one. The EXAFS analysis is less accurate, giving a smaller bond angle, even if compatible with the XANES results.

The Mn-Ca_1 distributions found by EXAFS, XANES, and diffraction analysis are in good agreement as also shown in Fig. 4: the average distance and variance are similar, even if the EXAFS distance is slightly reduced. In addition the XANES analysis points out an asymmetric Mn-Ca_1 distribution, in very good agreement with the diffraction results.

Our accurate analysis of the EXAFS data allows some insight also into the medium-range order. The main structural contributions are associated with the Mn_2 (diagonal of the cube faces), with the O_3 ions (opposite cube edges), and with the Mn-Ca_1-Mn_3 configurations along the cube edges. The atomic distances derived from the analysis are, however, only in rough agreement with the average crystallographic structure, because at such long distance the structural information is weak due to the large structural disorder and the quite large number of possible structural contributions that should be considered. In this medium-range region the

TABLE II. The main structure features characterizing the Mn local atomic environment in $CaMnO_3$ and $LaMnO_3$ samples as obtained from XANES structural refinement.

$R_{Mn—O}\pm0.02$ (Å)	$\theta_{MnO_1Mn_1}\pm5$ (deg)	$R_{MnCa/La}\pm0.04$ (Å)
	$CaMnO_3$	
1.90	149	3.02
1.90	151	3.11
1.91	159	3.12
1.92	164	3.21
1.93	163	3.22
1.93	169	3.30
		3.33
		3.36
	$LaMnO_3$	
1.93	149	3.23
1.93	153	3.25
1.94	158	3.25
1.94	161	3.41
2.10	163	3.49
2.10	165	3.55
		3.78
		3.82

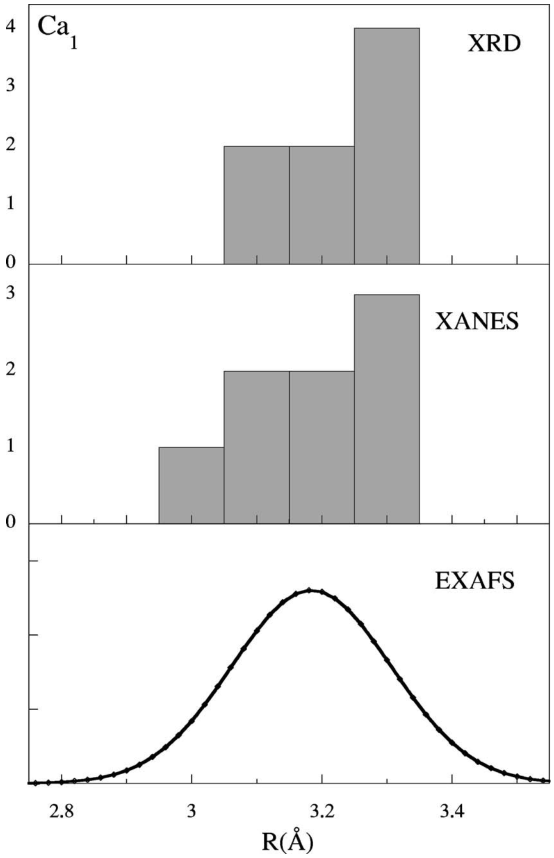

FIG. 4. Pictorial view of the Mn-Ca_1 and distributions as derived from diffraction data (upper panels) compared with XANES (middle panels) and EXAFS (lower panels) results.

TABLE III. The main structural features of $LaMnO_3$ and $CaMnO_3$ samples as obtained by EXAFS and XANES analyses are compared with the crystallographic structure.

	Crystal	EXAFS	XANES
		$CaMnO_3$	
$\bar{R}_{O_1}$ (Å)	1.90	1.895	1.914
σ_{JT} (Å)	0.01	-	0.01
$\bar{\theta}_{O_1}$ (deg)	159.2	156.6	159.1
$\bar{\sigma}_\theta$ (deg)	4.8	-	7.9
$\bar{R}_{Ca_1}$ (Å)	3.23	3.18	3.21
$\bar{\sigma}_{Ca_1}$(Å)	0.09	-	0.12
		$LaMnO_3$	
R_{O_p} (Å)	1.938	1.925	1.934
R_{O_a} (Å)	2.174	2.13	2.10
$\bar{R}_{O_1}$ (Å)	2.017	1.99	1.99
σ_{JT} (Å)	0.125	0.096	0.084
$\bar{\theta}_{O_1}$ (deg)	155.3	161	158.1
$\bar{\sigma}_\theta$ (deg)	0.05	-	5.9
$\bar{R}_{La_1}$ (Å)	3.42	3.43	3.48
$\bar{\sigma}_{La_1}$ (Å)	0.18	-	0.24

XANES analysis becomes prohibitively long due to the correlation among the structural parameters involved. In the near future the possibility to enhance the computing speed (parallelization of the MXAN code) will probably allow us to extend the analysis also to this region.

In conclusion the XAS analysis of $CaMnO_3$ depicts an excellent agreement between EXAFS and XANES, demonstrating the consistence of the two analysis. The agreement between XAS and crystallographic structure is also good and demonstrates the accuracy of the MXAN approach. In the $LaMnO_3$ sample the main structural features derived from XANES and EXAFS are in good agreement too, confirming the consistency of the two methods even in this more complex case. EXAFS and XANES analyses show a bimodal distribution of Mn-O_1 distances with four nearest neighbors and two longer bonds. The shorter Mn-O_{1p} distances found by XAS analysis ($R_{O_p} \sim 1.93$ Å) are in good agreement with the crystallographic distance ($R_{O_p} \sim 1.94$ Å). However, the XANES analysis suggests all the planar oxygen ions to be at the same distance, differently from crystallographic structure which points out two well-defined distances at 1.905 Å and 1.968 Å. The average Mn-O_1 distance found from EXAFS and XANES is the same and slightly shorter than the crystallographic value. In particular both EXAFS and XANES give for the Mn-O_{1a} bond length shorter values with respect to the crystallographic data, particularly the XANES as highlighted in Fig. 5. Let us discuss with more details these re-

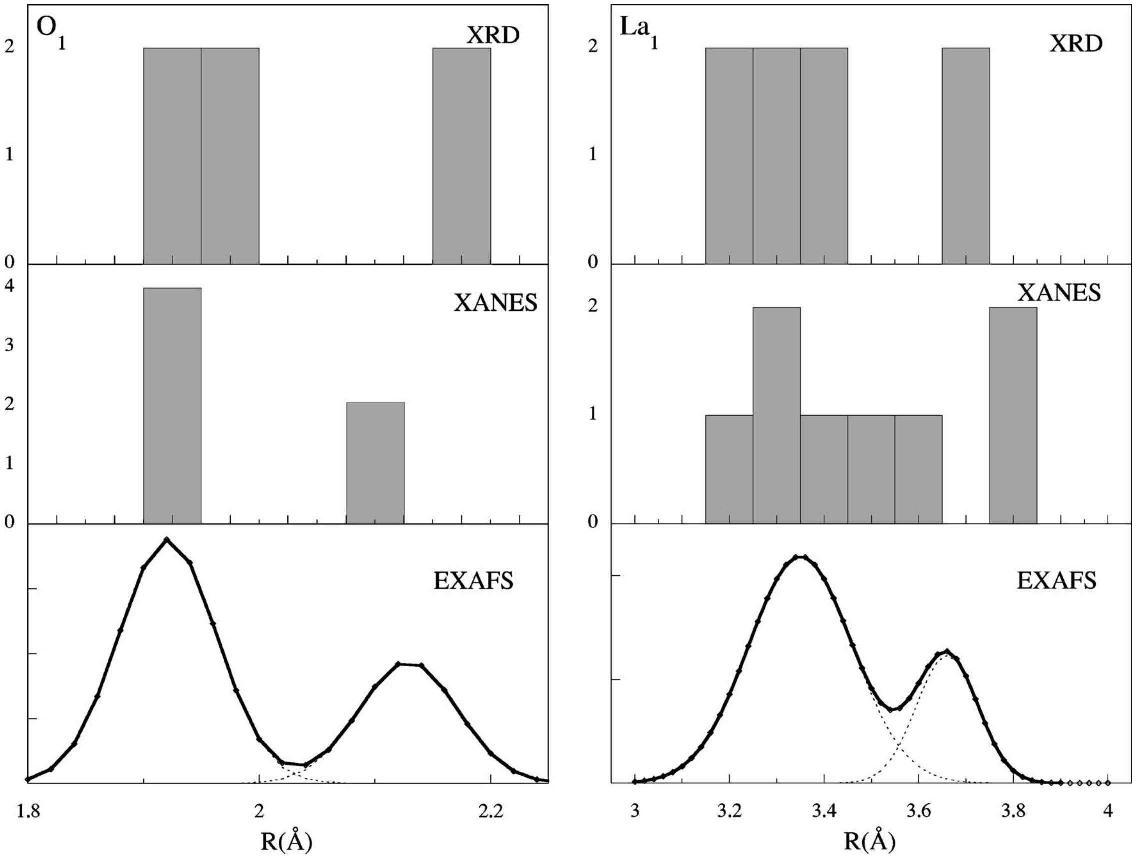

FIG. 5. Pictorial view of the Mn-O_1(left) and Mn-La_1 (right) distributions in $LaMnO_3$ as given from crystallography (upper panels) compared with our XANES (middle panels) and EXAFS (lower panels) results.

sults, since precise knowledge of the local structure in Jahn-Teller-distorted MnO_6 octahedra is relevant in the still open discussion on the peculiar physical properties of manganites. Discrepancies between XAS and diffraction results are often reported in the literature; they may arise from either physical or fictitious effects. In fact, on the one hand, large differences between local and long-range coherent structure are often documented in these compounds. On the other hand, systematic errors in the EXAFS data analysis may originate from the correlation between distances and energy scale parameters and the XANES results can be affected by the choice of interatomic potentials. We underline that in the present case the contraction is observed only for one distance, the long Mn-O_{1a} bond, while all the other structural parameters show a general agreement between crystallographic and XAS results. This points towards the true shorter distance of the Mn-O_{1a} atoms. We notice that a similar contraction of the apical Mn-O bond has been reported in Ref. 43 as a result of slightly not stoichiometric $LaMnO_3$ phases. Therefore the contraction of the apical Mn-O bond length can be partially due to local deviations from ideal stoichiometry in this sample.

Again XANES data show that the six O_1 neighbors are effectively in an octahedral configuration around Mn_0 with O_1-Mn_0-O_1 bond angles θ_{Mn_0} equal to 90°. with $\sigma^2_\theta \sim 4°$. The average Mn-O_1-Mn_1 bond angles (θ_{O_1}) found by XAS are slightly larger ($\sim 5°$) than the average crystallographic value; the XANES show a broad θ_{O_1} distribution with a bimodal trend (as for $CaMnO_3$ sample) with two smaller angles (around 151°) and four larger angles (around 162°). This finding differs from the sharp distribution of the crystallographic structure.

As shown in Fig. 5, the average Mn-La_1 distances found by XAS and diffraction are the same within the errors; both EXAFS and XANES show a bimodal distribution with six nearest La ions and two far away which is in quite good agreement with the crystallographic structure. We note only that XANES shows a long Mn-La distance slightly elongated with respect to EXAFS and XRD.

Also in this case the EXAFS gives some insight into the medium range order of $LaMnO_3$ showing features that can be ascribed to the Mn_2 ions (diagonal of the cube faces), Mn-La_2, and Mn-La_1-Mn_3, three ion configurations. Notice that the effect of oxygen ions (O_2 and O_3) is negligible in this case, probably due to the large structural disorder.

The Mn *K*-edge EXAFS and XANES data on $LaMnO_3$ are in good agreement. The local structure derived from the XAS analysis somewhat differs from the crystallographic structure, suggesting the existence of a difference in the actual local structure with respect to that inferred from crystallographic measurements.

The good results obtained in these two reference manganite compounds encourage us to extend this approach to doped manganites as well, in which the details of local structure are a fundamental issue for the full understanding of their peculiar magnetotransport properties. However, in the doped manganites two different sites are in principle present—the Mn^{3+} and Mn^{4+} sites—each one with its local structure; therefore, to fully characterize the local order and to get a reliable structural refinement from the XANES spectra, a large number of different contributions should be considered. This prohibitively enlarges the computation time, making this problem capable of being addressed only when a parallelized MXAN version is available.

ACKNOWLEDGMENTS

The GILDA project is financed by the Italian institutions CNR, INFM, and INFN. The very efficient technical support of F. Campolungo, V. Sciarra, and V. Tullio from the Laboratori Nazionali di Frascati (INFN) has been greatly appreciated. U.M. thanks CSIR, Government of India, for financial support.

---

*Corresponding author. Electronic address: meneghini@fis.uniroma3.it

[1] C. Zener, Phys. Rev. **82**, 403 (1951).

[2] P. Anderson and H. Hasegawa, Phys. Rev. **100**, 675 (1955).

[3] P. de Gennes, Phys. Rev. **118**, 141 (1960).

[4] A. J. Millis, P. B. Littlewood, and B. I. Shraiman, Phys. Rev. Lett. **74**, 5144 (1995).

[5] A. J. Millis, B. I. Shraiman, and R. Mueller, Phys. Rev. Lett. **77**, 175 (1996).

[6] B. Salamon and M. Jaime, Rev. Mod. Phys. **73**, 583 (2001).

[7] P. G. Radaelli, G. Iannone, M. Marezio, H. Y. Hwang, S. W. Cheong, J. D. Jorgensen, and D. N. Argyriou, Phys. Rev. B **56**, 8265 (1997).

[8] C. H. Booth, F. Bridges, G. J. Snyder, and T. H. Geballe, Phys. Rev. B **54**, R15606 (1996).

[9] D. Louca and T. Egami, Phys. Rev. B **59**, 6193 (1999).

[10] P. A. Lee, P. H. Citrin, P. Eisenberger, and B. M. Kinkaid, Rev. Mod. Phys. **53**, 769 (1981).

[11] A. Lanzara, N. L. Saini, M. Brunelli, F. Natali, A. Bianconi, P. G. Radaelli, and S. W. Cheong, Phys. Rev. Lett. **81**, 878 (1998).

[12] G. Subías, J. García, M. G. Proietti, and J. Blasco, Phys. Rev. B **56**, 8183 (1997).

[13] C. H. Booth, F. Bridges, G. H. Kwei, J. M. Lawrence, A. L. Cornelius, and J. J. Neumeier, Phys. Rev. B **57**, 10440 (1998).

[14] C. Meneghini, R. Cimino, S. Pascarelli, S. Mobilio, C. Raghu, and D. D. Sarma, Phys. Rev. B **56**, 3520 (1997).

[15] C. Meneghini, C. Castellano, S. Mobilio, A. Kumar, S. Ray, and D. D. Sarma, J. Phys.: Condens. Matter **14**, 1967 (2002).

[16] G. Subías, J. García, J. Blasco, M. C. Sánchez, and M. G. Proietti, J. Phys.: Condens. Matter **14**, 5017 (2002).

[17] G. Subías, J. García, J. Blasco, and M. G. Proietti, Phys. Rev. B **58**, 9287 (1998).

[18] M. Benfatto, Y. Joly, and C. R. Natoli, Phys. Rev. Lett. **83**, 636 (1999).

[19] F. Bridges, C. H. Booth, G. H. Kwei, J. J. Neumeier, and G. A. Sawatzky, Phys. Rev. B **61**, R9237 (2000).

[20] F. Bridges, C. H. Booth, M. Anderson, G. H. Kwei, J. J. Neumeier, J. Snyder, J. Mitchell, J. S. Gardner, and E. Brosha, Phys. Rev. B **63**, 214405 (2001).

[21] Q. Qian, T. A. Tyson, C. C. Kao, M. Croft, S. W. Cheong, G. Popov, and M. Greenblatt, Phys. Rev. B **64**, 024430 (2001).

[22] A. Y. Ignatov, N. Ali, and S. Khalid, Phys. Rev. B **64**, 014413 (2001).

[23] M. Benfatto, C. R. Natoli, A. Bianconi, J. García, A. Marcelli, M. Fanfoni, and I. Davoli, Phys. Rev. B **34**, 5774 (1986).

[24] J. J. Rehr and R. C. Albers, Rev. Mod. Phys. **72**, 621 (2000).

[25] S. I. Zabinsky, J. J. Rehr, A. Ankudinov, R. C. Albers, and M. J. Eller, Phys. Rev. B **52**, 2995 (1995).

[26] M. Benfatto and S. Della Longa, J. Synchrotron Radiat. **8**, 1087 (2001).

[27] M. Benfatto, S. Della Longa, and C. R. Natoli, J. Synchrotron Radiat. **10**, 51 (2003).

[28] M. Benfatto, P. D'Angelo, S. Della Longa, and N. V. Pavel, Phys. Rev. B **65**, 174205 (2002).

[29] P. D'Angelo, M. Benfatto, S. Della Longa, and N. V. Pavel, Phys. Rev. B **66**, 064209 (2002).

[30] S. Pascarelli, F. Boscherini, F. DAcapito, J. Hrdy, C. Meneghini, and S. Mobilio, J. Synchrotron Radiat. **3**, 147 (1996).

[31] A. L. Ankudinov, B. Ravel, J. J. Rehr, and S. D. Conradson, Phys. Rev. B **58**, 7565 (1998).

[32] K. R. Poeppelmeier, M. E. Leonowicz, J. C. Scanlon, and J. M. L. W. B. Yelon, Solid State Chem. **45**, 71 (1982).

[33] Q. Huang, A. Santoro, J. W. Lynn, R. W. Erwin, J. A. Borchers, J. L. Peng, and R. L. Greene, Phys. Rev. B **55**, 14987 (1997).

[34] *Error Reporting Recommendations: A Report of the Standards and Criteria Committee* (2000), URL http://ixs.csrri.iit.edu

[35] F. James, *CERN 506, Program Library* (1994).

[36] T. A. Tyson, K. O. Hodgson, C. R. Natoli, and M. Benfatto, Phys. Rev. B **46**, 5997 (1992).

[37] L. Hedin and S. Lundqvist, Solid State Phys. **23**, 1 (1969).

[38] J. E. Muller, O. Jepsen, and J. W. Wilkins, Solid State Commun. **42**, 365 (1997).

[39] A. Filipponi and A. Di Cicco, Phys. Rev. A **52**, 1072 (1995).

[40] A. Filipponi, A. Di Cicco, P. Pianetta, and T. Kendelewicz, Phys. Rev. B **53**, 15571 (1996).

[41] A. Filipponi, E. Bernieri, and S. Mobilio, Phys. Rev. B **38**, 3298 (1988).

[42] A. C. Thompson *et al.*, *X-RAY DATA BOOKLET* (Lawrence Berkeley National Laboratory, University of California, Berkeley, 2001).

[43] T. Shibata, B. A. Bunker, and J. F. Mitchell, Phys. Rev. B **68**, 024103 (2003).

[44] The MXAN code allows one to refine, at each run, the atomic coordinates of 12 ions at the maximum. In large systems these "free ions" must be suitably chosen and several runs must be reiterated.